Optical Engineering

OpticalEngineering.SPIEDigitalLibrary.org

Nanosatellite optical downlink experiment: design, simulation, and prototyping

Emily Clements
Raichelle Aniceto
Derek Barnes
David Caplan
James Clark
Iñigo del Portillo
Christian Haughwout
Maxim Khatsenko
Ryan Kingsbury
Myron Lee
Rachel Morgan
Jonathan Twichell
Kathleen Riesing
Hyosang Yoon
Caleb Ziegler
Kerri Cahoy

Emily Clements, Raichelle Aniceto, Derek Barnes, David Caplan, James Clark, Iñigo del Portillo, Christian Haughwout, Maxim Khatsenko, Ryan Kingsbury, Myron Lee, Rachel Morgan, Jonathan Twichell, Kathleen Riesing, Hyosang Yoon, Caleb Ziegler, Kerri Cahoy, "Nanosatellite optical downlink experiment: design, simulation, and prototyping," *Opt. Eng.* **55**(11), 111610 (2016), doi: 10.1117/1.OE.55.11.111610.

Nanosatellite optical downlink experiment: design, simulation, and prototyping

Emily Clements,[a,b,*] Raichelle Aniceto,[a] Derek Barnes,[a] David Caplan,[b] James Clark,[a] Iñigo del Portillo,[a] Christian Haughwout,[a] Maxim Khatsenko,[a] Ryan Kingsbury,[a] Myron Lee,[a] Rachel Morgan,[a] Jonathan Twichell,[b] Kathleen Riesing,[a] Hyosang Yoon,[a] Caleb Ziegler,[a,b] and Kerri Cahoy[a]
[a]Massachusetts Institute of Technology, Department of Aeronautics and Astronautics, Space Telecommunications and Radiation Laboratory, 77 Massachusetts Avenue, Cambridge, Massachusetts 02139, United States
[b]Massachusetts Institute of Technology, Lincoln Laboratory, 244 Wood Street, Lexington, Massachusetts 02420, United States

Abstract. The nanosatellite optical downlink experiment (NODE) implements a free-space optical communications (lasercom) capability on a CubeSat platform that can support low earth orbit (LEO) to ground downlink rates > 10 Mbps. A primary goal of NODE is to leverage commercially available technologies to provide a scalable and cost-effective alternative to radio-frequency-based communications. The NODE transmitter uses a 200-mW 1550-nm master-oscillator power-amplifier design using power-efficient M-ary pulse position modulation. To facilitate pointing the 0.12-deg downlink beam, NODE augments spacecraft body pointing with a microelectromechanical fast steering mirror (FSM) and uses an 850-nm uplink beacon to an onboard CCD camera. The 30-cm aperture ground telescope uses an infrared camera and FSM for tracking to an avalanche photodiode detector-based receiver. Here, we describe our approach to transition prototype transmitter and receiver designs to a full end-to-end CubeSat-scale system. This includes link budget refinement, drive electronics miniaturization, packaging reduction, improvements to pointing and attitude estimation, implementation of modulation, coding, and interleaving, and ground station receiver design. We capture trades and technology development needs and outline plans for integrated system ground testing. [DOI: 10.1117/1.OE.55.11.111610]

Keywords: free-space optical communication; laser communication; small satellite; CubeSat; master-oscillator power-amplifier; pulse position modulation.

Paper 160765SS received May 15, 2016; accepted for publication Jul. 26, 2016; published online Sep. 13, 2016.

1 Introduction

The increasing use of nanosatellites as host platforms for increasingly data-intensive sensors such as hyperspectral imagers or video, drives a need for more power-efficient, higher-rate data downlink capability. CubeSats, the dominant standard for nanosatellites, have limited size, weight, and power, making it difficult to accommodate high gain radio-frequency (RF) antennas. This pushes most CubeSat missions with high data rate needs to use ground stations with large, high-gain apertures (dish diameters ranging from 5 to 20 m). There are also regulatory challenges in obtaining RF licenses with substantial bandwidth for CubeSat missions; even management of the many narrow-bandwidth license requests has become an issue. An alternative to traditional RF communications is desirable for CubeSats.

1.1 *Rise of Nanosatellites*

The availability of low-cost launches has led to exponential growth in nanosatellite programs over the last 15 years.[1,2] Nanosatellites typically have a total mass of less than 10 to 15 kg and include standard CubeSat form factors (multiples of a 10 cm × 10 cm × 10 cm, 1.33 kg cube, or 1U) up to about 6U in size. These standardized satellites are launched in deployers such as those used by NanoRacks CubeSat Deployer Services.[3] While early nanosatellites were limited in performance, carrying only low size, weight, and power (SWaP) payloads such as magnetometers, the miniaturization of consumer electronics and research sensors has enabled more advanced payloads to fit on nanosatellites.[1] These satellites have been used for technology demonstrations such as microsized microwave atmospheric sounder,[4] commercial imaging ventures such as Planet Labs (name recently shortened to just "Planet") and scientific endeavors.[5,6] While we note that lasercom systems designed for nanosatellites may also have utility for microsatellites (mass of less than 50 kg[7]), in this work, we focus on CubeSats due to their dominance of the small satellite market.[7]

1.2 *Motivation for CubeSat Lasercom*

CubeSats now carry more advanced, power-intensive payloads that generate large amounts of data. Such missions are limited by their ability to downlink data using traditional, RF communication systems at ultrahigh frequency (UHF) with CubeSat tape-spring antennas.[8,9] For example, in Ref. 10, a multispectral imager on a 6U CubeSat is limited to 63 s of imaging because the S-band downlink at 14 Mbps consumes enough power that it can only be run for 10 min each orbit. RF downlink on CubeSats is limited by transmit power and the cost and availability of high-gain ground stations.[11] Because of these data rate demands, the maximum data rate of CubeSat RF communications has greatly increased in recent years, partly through switching to higher frequency bands and partly through using higher gain ground stations. According to Klofas and Leveque,[12] the highest RF

*Address all correspondence to: Emily Clements, E-mail: eclements@mit.edu

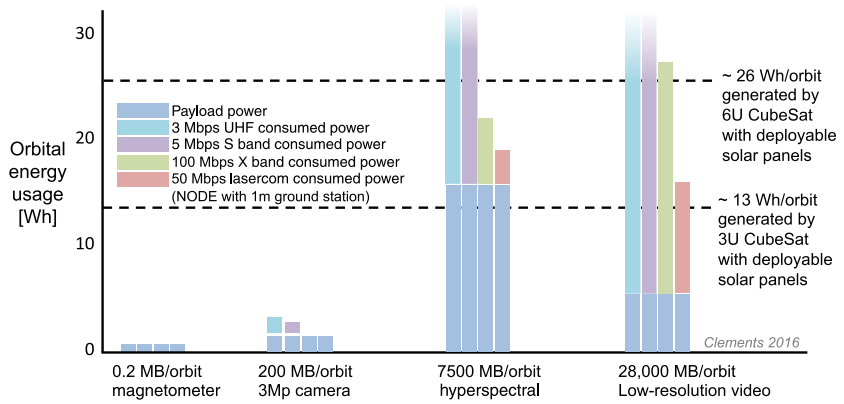

Fig. 1 Power consumption of possible payloads for LEO CubeSats compared with power consumption for downlinking the payload data with different CubeSat communication systems. RF power consumption and data rates are based on commercial products[6,15,16,17] and power generation is based on an example CubeSat mission.[4] The payload data are based on scaling the duty cycle of recent or proposed missions and payloads.[9,18,19–21]

CubeSat data rate as of 2013 was 2.6 Mbps using the L3 Cadet UHF radio; since then, the maximum data rate achieved was 100 Mbps using an X-band system.[6] Other high-data-rate demonstrations are in formulation such as the Aquila Space Ka-band system with expected performance of 200[13] up to 320 Mbps[14] and X-band systems such as those from Tethers Unlimited with over 100 Mbps.[15] However, to achieve these data rates, higher power transmitters or higher gain ground stations are required, and the RF licensing process is lengthy.[8,12]

Laser communications (lasercom) offers an attractive alternative to RF communications for nanosatellites because of the power efficiency of high data rate transmissions. Figure 1 shows the utility of lasercom systems for two example advanced payloads (a hyperspectral imager and a video camera) and the lack of need for lasercom for two more traditional CubeSat payloads (a magnetometer and a low-resolution camera). The magnetometer and the low-resolution camera, even when operating at 100% duty cycle, do not produce enough data to challenge UHF communication systems. However, a hyperspectral imager as in Mandl (2015) consumes 10 W of power and produces over 10 Mbps of data.[18] If run at 100% duty cycle, this hyperspectral imager can consume more power than a 3U CubeSat can produce; even a 6U CubeSat is challenged. For example, a 3U CubeSat may generate 13 W-h of power per orbit,[4] while a hyperspectral imager may consume 10 W-h per orbit.[18] Even if a system had enough ground stations that access time did not limit communications, the power of the CubeSat payload plus RF communications system would limit the payload duty cycle.

1.3 *Nanosatellite Optical Downlink Experiment Overview*

In this paper, we describe the nanosatellite optical downlink experiment (NODE), which is a low-cost, commercial off the shelf (COTS)-based lasercom downlink payload being designed and built at the Massachusetts Institute of Technology.[22–28] NODE will demonstrate a direct detection architecture, a fast steering mirror (FSM) to augment coarse bus pointing control, and an uplink beacon to aid bus pointing knowledge. The NODE demonstration is designed both to demonstrate low-SWaP downlink (greater than 40 Mbps to a 1-m telescope or 10 Mbps to a 30-cm telescope) and to characterize performance through built-in self testing and mirror feedback. This paper expands on the results presented in Ref. 22 by contributing details on implementation of the design and system-level developments toward the NODE demonstration. The NODE system consists of a transmitter payload on board a commercial spacecraft, referred to here as the "host," and two possible ground terminals equipped with a COTS avalanche photodiode detector (APD) and electronics that will store and later demodulate the signal. In addition to the planned 30-cm amateur telescope (AT) with augmented tracking capability and receive components including an APD, NODE may also downlink to the National Aeronautics and Space Administration (NASA) Jet Propulsion Laboratory (JPL) Optical Communications Telescope Laboratory (OCTL) telescope (1-m class), also equipped with an APD and NODE receive electronics. The OCTL option can test higher data rates, while the AT will be tested as a low-cost lasercom ground station alternative. The transmitter uses 1550-nm COTS parts and a master-oscillator power-amplifier (MOPA) architecture to generate 0.2 W transmit power collimated to a modest 2.26 mrad. NODE is designed to accommodate the pointing capabilities and mission constraints of the host, so the pointing control uplink beacon is in a bistatic configuration, with the beacon receiver integrated with the host camera due to the volume constraints of the host. It would be advisable to revisit the bistatic versus monostatic configuration for different host constraints. Additional details on the concept of operations can be found in Refs. 22, 25, and 28.

1.4 *Paper Organization*

The following sections describe the NODE simulation, design, and hardware in the loop experiments. In Sec. 2, we describe the state-of-the-art nanosatellite laser communications demonstrations and related work, including previous space-based lasercom demonstrations, missions in development, and key technologies. In Sec. 3, we describe a new probabilistic approach to lasercom link analysis that allows us to model the effects of uncertainties in the system and

prioritize modeling and test efforts. In Sec. 4, we build on work by Kingsbury[22] and describe the design approach and prototyping of the electronics and packaging for the transmitter and receiver.

2 Background

While lasercom has been demonstrated on missions such as the Lunar Laser Communication Demonstration (LLCD),[29] there are unique challenges in developing a laser communications system for the limited SWaP available for CubeSats that can compete with and outperform existing RF solutions while also maintaining the COTS and low-cost philosophy that permeates the CubeSat landscape. In the following sections, we describe key developments in lasercom for microsatellites and CubeSats. We also include some components relevant to lasercom that have been flown for other mission applications (e.g., laser altimetry, laser ranging, and lidar). We attempt to briefly capture the basic relevant information here, along with recent mission concepts and status updates since Kingsbury,[22] and refer the reader to that thesis for more detail.

2.1 *Previous Space-Based Lasercom Demonstrations*

Laser communications from space have been demonstrated by several missions with larger satellites. For example, in 2005, the Optical Inter-Orbit Communications Engineering Test Satellite (OICETS), a 570-kg satellite, demonstrated intersatellite lasercom links using the Laser Utilizing Communications Equipment (LUCE) in cooperation with the Advanced Relay and Technology Mission (ARTEMIS) satellite. LUCE was a 140-kg, 220-W payload, operated at 847 nm, and used on-off keying (OOK) to crosslink at nearly 50 Mbps.[30] More recently, in 2013, LLCD on the Lunar Atmosphere and Dust Environment Explorer (LADEE) demonstrated up to 622 Mbps from lunar orbit using a 0.5-W, 15-μrad beam at 1550 nm.[29] Lasercom technology continues to be integrated with space platforms, such as the Optical Payload for Lasercomm Science (OPALS), a payload on board the International Space Station (ISS), which demonstrated up to 50 Mbps downlink using a 1550-nm 1-W beam and a 976-nm uplink beacon for pointing knowledge to the OCTL 1-m telescope. The Lunar Communication Relay Demonstration (LCRD) extends the work of LLCD to geo-stationary applications.[31] Technology readiness level development is underway at NASA on the Deep Space Optical Terminal program.[32] Finally, 10-Mbps lasercom was recently demonstrated from a Low Earth Orbit (LEO) micro-satellite in the Small Optical Transponder (SOTA) experiment.[33]

2.2 *Programs in Development*

In this section, we summarize ongoing efforts to develop CubeSat lasercom systems, related technologies, and lasercom ground support systems.

2.2.1 *CubeSat lasercom*

There are several other efforts to develop lasercom systems and modules for CubeSats. The Aerospace Corporation (referred to as "Aerospace" for brevity in this work) is developing the Optical Communications and Sensor Demonstration (OCSD), which will demonstrate over 5 Mbps downlink to 30 and 80 cm ground stations with a 10-W 1064-nm beam.[34,35] OCSD will body-point their planned 0.2-deg beam.[34,35] Compact modulators for high data rate CubeSat lasercom are in development that plan to use differential pulse position modulation to improve power efficiency of the laser signal.[36] Fibertek is developing a 1U CubeSat terminal for deep-space as part of the NASA small business innovation in research program,[37–39] and other interplanetary lasercom work is also underway at NASA by Kovalik et al.[40]

2.2.2 *Recent developments in industry*

Ground support systems for lasercom are an active area of work. BridgeSat, a new communications company, has partnered with Surrey to develop small satellites and a network of lasercom ground stations for satellite downlink use.[41,42] Fibertek is also developing modular ground stations for space-based lasercom systems that are scalable to hundreds of Gbps.[43] Additionally, the technology readiness level of advanced compact lasercom systems continues to improve in research laboratories.[44]

Technologies related to CubeSat lasercom such as CubeSat-based lasers for other applications[45–47] and detectors that could be used for lasercom crosslinks[48] are in development. Several mainstream media articles have documented the growing interest in lasercom for unmanned aerial vehicles at companies such as Google and Facebook for remote internet access, which would have similar payload SWaP constraints to CubeSats, and demonstrations are under way.[49–51] For example, the Google Loon program has demonstrated 155 Mbps over a 100-km range between two balloons under diverse conditions.[52]

2.3 *Key Enabling Technologies*

The key enabling technologies for CubeSat lasercom are improved pointing control for both the CubeSat and ground terminal, power efficiency, and compact electronics and packaging.

In order for lasercom on CubeSats to be competitive with RF solutions, the spacecraft terminal needs to be able to point a less than 5 mrad beam with a high slew rate (1 deg/s) despite uncertain spacecraft moments of inertia. (An initial lasercom demonstration with this modest beamwidth would help to define a path toward much more efficient, higher-bandwidth systems that could support higher rates with 100 μrad beams.) Most CubeSats use attitude determination systems that cannot achieve this level of control, although significant efforts are underway to incorporate low-cost star trackers onto CubeSats.[53] CubeSat laser communication systems must therefore be able to accommodate coarse bus attitude control. In contrast, the beamwidths necessary for high data rate downlinks with low power are shown in the lower left corner of Fig. 2. The demonstrated state-of-the-art in CubeSat control, as shown in Table 1, includes degree-level pointing control on several missions[54–57] and 45 arc sec (0.2 mrad) pointing in the Bright Target Explorer (BRITE) constellation,[58] but the arcsecond pointing application was for staring at fixed distant objects (stars). While propulsive maneuvers requiring precise pointing have been demonstrated,[61,62] this level of attitude control performance has not been reported during slew maneuvers similar to what would be required for LEO lasercom downlinks. Another challenge for CubeSat lasercom is power efficiency, given the limited power available to the host

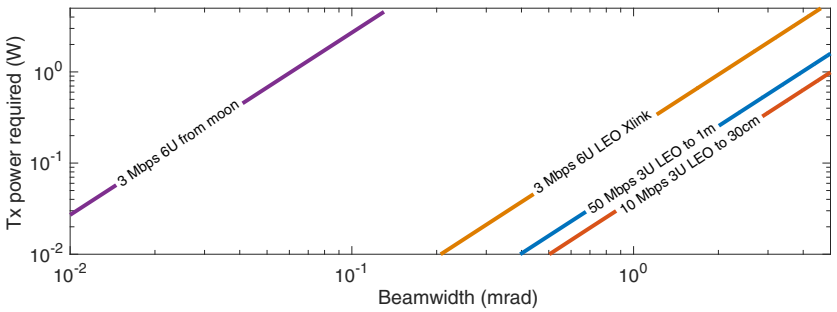

Fig. 2 Pointing requirements for CubeSat lasercom for LEO downlink from 475 km orbit, LEO crosslink, and lunar downlink applications. This figure assumes the architecture of each system follows the design described in this paper. The lunar downlink assumes a 1-m ground telescope and a 400,000 km range. The crosslink assumes a 1000-km range and a 8.5-cm receive aperture. All three concepts (LEO downlink, crosslink, and lunar downlink) assume the use of COTS APDs. The links were modeled following the link budget described in Sec. 3.1.

Table 1 List of recent and upcoming missions and their pointing control capabilities. While only the BRITE mission has carried star trackers to date with published results, many near-term missions expect to demonstrate the use of star trackers for advanced pointing control.

Mission	Year	Org.	Pointing	Notes
Recent				
CANX-2	2008	U. of Toronto	2 deg, 1σ	Not during slew maneuvers[54]
PSSCT-2	2011	Aerospace	15 deg, 3σ	Not during slew maneuvers[55,56]
Aerocube	2012	Aerospace	3 deg, 3σ	Not during slew maneuvers[57]
BRITE	2014		0.0115 deg	Star tracker, astronomical observations[58]
MinXSS	2016	UC Boulder	0.002 deg, 1σ	Using BCT XACT[59,60]
Upcoming				
OCSD	2016	Aerospace	0.1 deg	Pointing while ground tracking[34]

spacecraft. Per the design trades discussed by Kingsbury, space-rated erbium-doped fiber amplifiers (EDFAs) are available, but do not fit the SWaP constraints of CubeSats. Commercially available EDFAs used in the telecommunications (telecom) industry, however, are available that meet the SWaP constraints.[22] The use of COTS parts, if they can meet the power requirements of the space terminal and survive in the space environment for the CubeSat mission lifetime (typically less than 5 years) helps to keep the cost low.

Another enabling factor for space-based lasercom systems is the development of a geographically diverse ground station network to ensure reliability of access, because weather can temporarily block transmission of optical signals. Previous laser communication demonstrations have used large ground receive telescopes, such as OCTL[63] or several smaller apertures, such as lunar lasercom ground terminal (LLGT).[29,64] Such terminals, which also tend to use very sensitive detectors, such as superconducting nanowire single-photon detectors, are expensive to build and maintain, and fielding enough ground stations to support a mission's desired availability may prove prohibitively expensive. To make near-real-time access to downlinked data a possibility, we have developed a receive telescope based on 30-cm-diameter amateur telescopes with COTS detectors.

3 Modeling and Simulation

In this section, we present two aspects of NODE simulation: link analysis and pointing simulation.

3.1 *Link Modeling and Simulation*

Using traditional, deterministic analysis approaches, which calculate link margin using conservative estimates of inputs, can result in lasercom system designs that do not optimize data rate.[65] This is particularly applicable for CubeSat lasercom systems, in which uncertainties are especially large because of COTS parts and unknown mission parameters, and conservatism is less necessary because risk is more easily tolerated compared with larger systems. In this section, we present a link analysis with preliminary uncertainty quantification and propagation, and a sensitivity analysis based on the approach by Saltelli et al.[66] and Stout[67] to guide next steps in modeling and test efforts. A comparison with previous deterministic link results described by Kingsbury[22] highlights the potential for higher performance using the uncertainty-based approach.

From Ref. 68, the equation for approximating channel capacity is

$$C = \frac{1}{\log(2)E_\lambda} * \left(\frac{P_{\text{req}}^2}{\frac{P_{\text{req}}}{\log(\text{PPM})} + \frac{2P_n}{\text{PPM}-1} + \frac{P_{\text{req}}^2 * \text{PPM} * T_s}{\log(\text{PPM}) * E_\lambda}} \right), \quad (1)$$

where C is the channel capacity in bits per second, P_{req} is the power required for a particular data rate in Watts, pulse position modulation (PPM) is the order of the pulse position modulation (a power of two between 8 and 512), T_s is the slotwidth of the PPM in seconds (we use 5 ns), and E_λ is the energy of a photon in Joules. The NODE system operates at $\lambda = 1550$ nm so the energy per photon is 1.28×10^{-19} J.

Equation (1) describes the "channel" bits per second. The actual rate of data transmission relates to the channel capacity combined with "taxes" for error-correcting bits, acquisition headers, intersymbol guard time, and data framing. It is more common for these to be accounted for in the received or required power calculations, and one would maintain a constant data rate and average power but increase the slotwidth/decrease the power per slot to compensate for the added bits. However, in our system, the slot width is fixed However, in our system, the slot width is fixed. Per Kingsbury,[22] decreasing the slot width challenges the bandwidth of the COTS APD, and increasing the laser slot width causes a poor extinction ratio. Decreasing the slot width would also decrease the power per slot at the APD beyond acceptable limits. Also, by deciding to maintain a constant slot rate, clock synchronization is easier. Therefore the power per slot remains the same, but the data rate is decreased as the miscellaneous coding bits are added, as shown in Table 2.

The margin of the link for each data rate is defined as the difference between power received and power required in decibels (dB). The received power (in dB) is the transmitted power plus gains from transmit and receive telescopes minus losses from various sources (such as transmitter and receiver optics, free-space loss, atmospheric loss, and pointing loss).

$$P_{\text{rec}} = P_{\text{T}} + G_{\text{T}} + G_{\text{R}} - L_{\text{T}} - L_{\text{R}} - L_{\text{FS}} - L_{\text{atm}} - L_{\text{pointing}}. \quad (2)$$

P_{T} is the transmit power, G_{T} is the transmitter gain, G_{R} is the receiver gain, L_{T} is the transmitter optical loss, L_{R} is the receiver optical loss, L_{FS} is the free-space loss, L_{atm} is the atmospheric loss, and L_{pointing} is the pointing loss.

Table 2 List of scaling factors used to estimate the data bit rate from the channel bit rate. Because NODE uses a constant slot width, the link budget scales the data rate instead of the power and slot width to account for error correcting bits and other factors.

Parameter	Data rate scaling factor	Rationale
RS error correction	239/255	Using a (239,256) RS code
Acquisition header	995/1000	5 ms/s for modulation framing
Intersymbol guard time	PPM/PPM + 1	One guard slot per symbol
Dataframe	0.98	2% overhead
Combined scaling	0.81 to 0.91	Product of above for various PPM

Atmospheric loss is a function of loss from absorption by water vapor. On a cloudy day, atmospheric loss will be too high to permit an optical link. On a perfectly clear day when the satellite is directly overhead, this loss can be as low as 0.5 dB. Future work will include a detailed MODTRAN analysis of expected atmospheric loss for NODE.

The required power (in dB) is

$$P_{\text{req,dB}} = 10 \times \log_{10}(P_{\text{signal,W}}) - L_{\text{imp}}, \quad (3)$$

where $P_{\text{signal,W}}$ is the required average signal power in Watts to differentiate from noise at a given bit error rate (BER), and L_{imp} is an implementation loss. This loss was measured to be ~3 dB based on benchtop measurements described by Kingsbury,[22] which we treat as a lower bound on implementation loss in case moving from a benchtop setting to a packaged flight setting causes additional implementation losses.

The average power is a function of the power required for an "on" slot and the power ratio of the peak to average power, both of which are a function of both signal power and noise power.

$$P_{\text{signal,W}} = \frac{\frac{\mu_{\text{ion}_{\text{req}}}}{(M_{\text{APD}} \times R_{\text{APD}})} - P_{\text{background}}}{PR_{\text{peaktoave}}}. \quad (4)$$

3.1.1 *Common lasercom losses that do not affect NODE*

There are several losses commonly found in lasercom link budgets that do not affect the current NODE system. (i) Detector blocking loss: this applies to Geiger Mode APDs (GM-APDs), but the NODE APD is linear mode. (ii) Coding gain/loss: as described in Sec. 3.1, the NODE slotwidth is fixed, so additional bits for coding do not affect the received power but rather impact the overall data rate. (iii) Interleaver efficiency: same reason as coding gain/loss. (iv) Truncation loss: this refers to optical truncation. The optical truncation at the receiver is book-kept by scaling the receiver area to account for the blocking by the secondary mirror. The transmitter does not have a truncation because the transmit aperture is wider than the beamwidth. (v) Scintillation loss: because of aperture averaging, in which the aperture is large enough that the variation in power across the area of the aperture average out the effects of scintillation, NODE does not encounter significant scintillation loss. According to Ref. 69 (p. 496), a 30-cm receive aperture is beyond the knee in the curve of the scintillation index, so scintillation loss is negligible.

3.1.2 *Deterministic link budget simulation results*

Table 3 compares the low data rate predicted using the in-progress AT ground station with a higher data rate using the OCTL ground station. We used conservative estimates in each row for the new analysis to be consistent with the deterministic analysis reported by Kingsbury.[22] Because this is a technology demonstration experiment, the result of less than 1 dB of margin for the 1000-km link to the AT suggests that low elevation angle test conditions may be challenging to close at times, and this may provide a set of stressing conditions to examine BER variation and system

Table 3 Comparison of link margin for the initial NODE demonstration for two different ground stations, 1-m aperture OCTL, and a 30-cm aperture AT. Note that the data bit rates include scaling factors such as error correction bits and header bits.

Input parameters	Amateur telescope	OCTL	Units	Notes
Channel data rate	9.9	43	Mbps	Constant slot rate of 2.00E + 08 Hz
PPM order	128	16		
Laser transmitter				
Average optical output power	0.20	0.20	W	Unchanged transmitter architecture
Laser wavelength	1550	1550	nm	
Extinction ratio	42	42	dB	Kingsbury measurements[22]
Half-power beamwidth	2.260	2.260	mrad	Selected flight collimator
Receive telescope and optics				
Focal length	2.8	75.8	m	AT datasheet,[70] OCTL paper[71]
Aperture diameter	27	100	cm	Scaled AT to account for secondary mirror
Background noise				
FoV	7.14E-05	2.64E-06	rad	
Sky spectral radiance	6.00E-04	6.00E-04	$W/cm^2 \times SR \times \mu m$	Originally from Hemmati[72]
Optical filter bandwidth	1	1	nm	
Receiver electronics				
APD gain	20	20	—	
Responsivity	1.0	1.0	A/W	Measured value from Kingsbury[22]
Excess noise factor	4.3	4.3		From device sales sheet via Kingsbury[22]
Noise equivalent power	2.80E-09	2.80E-09	W	From device sales sheet via Kingsbury[22]
Noise equivalent bandwidth	3.00E + 08	3.00E + 08	Hz	Larger than signal bandwidth Kingsbury[22]
Link budget summary				
Laser avg. optical power	−7.0	−7.0	dBW	
Transmit optical losses	−1.5	−1.5	dB	Accounting for 0.3 dB per planned splice
Transmit antenna gain	65.0	65.0	dBi	
Pointing loss	−3.0	−3.0	dB	
Path loss at 1000 km	−258.2	−258.2	dB	
Atmospheric loss	−1.0	−1.0	dB	
Receive antenna gain	114.7	126.1	dB	
Receive optics losses	−2.0	−3.0	dB	AT assumes −1 dB for beamsplitter plus miscellaneous losses; OCTL has higher losses due to more complicated optics
Receiver Implementation loss	−3.0	−3.0	dB	Measured value from Kingsbury[22]
Signal power at detector	−92.95	−82.6	dBW	
Signal power req'd, BER = 1e-4	−93.2	−84.2	dBW	Includes implementation loss
Margin at 1000 km	0.23	1.62	dB	Maximum range
Margin 600 km	3.04	4.30	dB	Nominal range

Table 4 Input distributions for Monte Carlo analysis. The distributions are uniform in scalar units rather than decibel units.

Variable	Value	Rationale
Pointing error	$N(0, 0.35)$ mrad	Sum of various errors from preliminary pointing budget for precalibration case, so normal distribution is assumed (postcalibration has negligible uncertainty)
HPBW	2.26 mrad $\pm$ 1%	Per collimator datasheet[75]
Tx optical losses	$N(-1.5, -0.5)$ dB	Assumes 0.3 dB per splice plus 0.5 dB for miscellaneous losses
ER	$U(6.31 \times 10^{-5}, 1.58 \times 10^{-4})$	Reported in Kingsbury that ER varied between −38 and −42 dB[22]
AT Rx optics losses	$U(0.5, 0.8)$	−1 dB for beamsplitter (not yet selected), −2 dB for other miscellaneous losses
OCTL Rx optics losses	$U(0.35, 0.5)$	
$L_{implementation}$	$U(0.4, 0.5)$	Kingsbury measured −3 dB in a benchtop test[22]

performance. This link budget will vary based on the atmospheric conditions at the time of experiment because of atmospheric losses and seeing. An atmospheric loss of 1 dB or better is expected about 70% of the time at zenith at Table Mountain, where we plan to operate, based on Nugent et al.,[73] or 60% of the time at 20 deg above the horizon if scaling the zenith cumulative distribution from Nugent using the Beer–Lambert law. Occasionally, the D/r_0 parameter may cause losses because of seeing; however, statistics of r_0 from Aliss and Felton[74] gives a worst-case (5%) r_0 of about 7 cm for Table Mountain at zenith (roughly 3.7 cm at lower elevation angles). With an APD diameter of 200 μm, an AT focal length of 2.8 m, and a diameter of 30 cm, the ratio D/r_0 is only 8.2, while the spot on the APD could grow by 11 times before overfilling (i.e., received signal spot size is larger than the detector and the portion that falls outside of the detector is lost). In contrast, OCTL has a focal length of 75.8 m and a diameter of 1 m; therefore, the spot can only grow by 1.4 times before overfilling without a focusing lens, yet D/r_0 is 27.2, so refocusing optics will be required similar to what was used on LLCD.[63]

We note that 73 Mbps is an upper bound on possible data rate with this component selection based on limitations of the hardware and software. (The architecture is scalable by design.[22]) Even if margin were available, such as through use of more sensitive detectors or larger aperture ground stations, using 4-PPM and the desired slot width (5 ns for this system for reasons described in Sec. 3.1) prevents scaling to higher data rates, so future work should include investigating the constraints of the transmitter optical subassembly (TOSA). Improved designs that can leverage wavelength division multiplexing (WDM) or more scalable modulation formats such as frequency shift keying could also improve the data rate.

3.1.3 *Probabilistic link budget simulation results*

We modeled the link uncertainties using Monte Carlo analysis, which gives insight into the probability of having negative margin, rather than the traditional approach which gives a pass/fail estimate of having more than 3-dB margin. Then we used two kinds of sensitivity analyses, local/gradient and global sensitivity analyses, to prioritize testing. The input distributions used in the initial Monte Carlo analysis are given in Table 4. The Monte Carlo uncertainty analysis results, shown in Fig. 3, estimate a high probability of positive margin for both OCTL and the AT, but the low elevation angle cases show a moderate chance of negative link margin for the 10 Mbps to the AT, and they indicate margin as expected is higher for overhead transmission than for links near the horizon (20-deg elevation angle), when the free-space loss would be greater. OCTL is able to have positive margin when receiving higher data rates than the AT ground station.

Motivation for performing a sensitivity analysis includes: (i) to find the sensitivity of the value of a parameter through gradient sensitivity analysis to inform redesign decisions and (ii) to find the sensitivity of the variance, or uncertainty, of a parameter through a global, variance-based sensitivity analysis to inform testing prioritization. To assess the gradient sensitivities, we varied each input parameter by 1% to perform a standard gradient sensitivity analysis, and then ranked the inputs based on the absolute value of the slope of the link margin. We use global sensitivity analysis to investigate key inputs under the marginal conditions at the horizon to prioritize testing and detailed modeling efforts as the program approaches system integration and test. The global sensitivity approach is based on Chapter 4 of Ref. 66, which defines sensitivity, S_i, as

$$S_i = \frac{\mathrm{Var}[E(Y|X_i)]}{\mathrm{Var}(Y)}, \tag{5}$$

where Y is the quantity of interest and X is the input of interest. $E(Y|X_i)$ gives the expected value of Y given a known value for X_i. A Monte Carlo analysis was used to determine the distribution, and therefore the variance, of Y (in this case, the link margin). A Monte Carlo analysis was then used to find the expected value of Y given a particular value for each input and the distribution of other inputs, and this was repeated for each possible value of each input. The variance of the resulting distribution for each input was taken to find $\mathrm{Var}[E(Y|X_i)]$.

We analyzed inputs currently thought to be changeable or testable: pointing error, beamwidth, transmitter and receiver optics losses, extinction ratio, and implementation loss. As shown in Fig. 3, we find that receiver optics loss is the biggest contributor to margin uncertainty, followed by transmitter optical losses, implementation loss, and pointing error. We found that the extinction ratio and half-power beamwidth

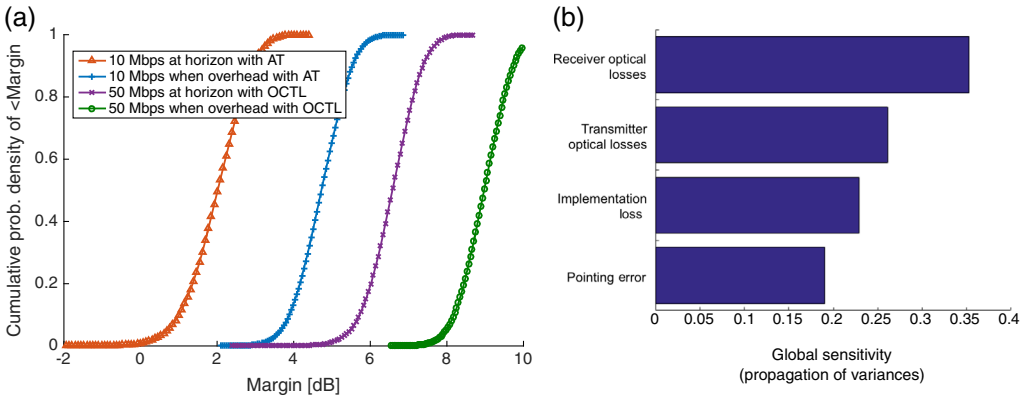

Fig. 3 (a) Monte Carlo results show the link margin cumulative density function (CDF) when communicating at different data rates to one of the two ground stations when the satellite is either overhead or close to the horizon (about 20 deg above), assuming a moderate range of atmospheric conditions. We propagated the uncertainties using Monte Carlo analysis with 2000 runs. (b) Then we ran a global sensitivity analysis of link with the AT pointing toward the horizon.

uncertainties had a negligible effect on the margin uncertainty. Gradient sensitivity analysis of both OCTL and the AT configurations assuming 1000-km range indicates pointing loss is the biggest contributor to the link margin, followed by implementation loss, half-power beam width, transmitter optics loss, and extinction ratio, indicating that a small change in pointing error or beamwidth will have the greatest effect on improving link margin. Moving forward, we will increase our emphasis on measuring optics losses, and we will use the gradient results, should any design changes be required.

3.2 *Spacecraft Pointing*

NODE is designed to support CubeSats with an initial pointing accuracy of ± 3 deg (3-σ) and the capability to slew at up to 1 deg/s to enable ground tracking from a 400-km orbit. NODE improves the bus pointing to ± 1 deg (3-σ) with beacon tracking, which allows an overlap with the fine steering stage range so that fine corrections can be applied. The optical beam deflection will be up to twice as much as the range depending on the optical configuration, so this ensures that the fine steering mechanism will not be operating near saturation. The second requirement of the fine stage is that it provides steering accuracy to ± 1.05 mrad (3-σ), which limits its pointing loss to 3 dB or less.

Two simulations were developed to assess the pointing performance of NODE in Ref. 28. Neither of these simulations model position feedback from the FSM; this is an item for future work. We summarize the results from both simulations here but only describe the first simulation in detail. The first simulation models the postacquisition tracking performance of the system. If the host satellite achieves initial pointing within the required ± 3 deg of the ground station, the beacon can be acquired instantaneously. This simulation begins at the moment of acquisition of the ground station and models the pointing performance of a representative CubeSat bus as well as the performance of the fine stage. Without Tx/Rx path misalignment and without feedback on the FSM position, the predicted pointing performance of NODE is 0.18 mrad (3σ). The second simulation, described in more detail in Ref. 28, focuses on calibration of the Tx/Rx alignment. Algorithms for the elimination of pointing bias are assessed to ensure that any on-orbit misalignment can be corrected. Results of this simulation indicate that Tx/Rx path misalignment can be reduced to 0.11 mrad or less. Combining results from both simulations, the predicted performance of NODE is ± 0.3 mrad (3-σ), which meets the ± 1.05 mrad fine pointing requirement with significant margin. In addition to this analysis, tests to characterize the response of the mirrors under the expected thermal range have been conducted, which are described further in Sec. 4.1.2.

The simulation consists of sensors, actuators, and software for estimation and control for the fine and coarse stages. The block diagram of the simulation is shown in Fig. 4. The coarse stage models a CubeSat bus with a reaction wheel actuator and gyroscope sensor. Precise position feedback is provided by the beacon detector on NODE. The fine stage FSM actuator is modeled to augment coarse pointing. The outer loop in Fig. 4 is the coarse pointing, which occurs at a rate of 4 Hz, while the inner fine pointing loop occurs at a rate of 10 Hz. Sources of error are included from sensors, actuators, and dynamics (which includes environmental disturbances, orbital knowledge, and knowledge of inertial attributes). The NODE beam is sufficiently wide that point-ahead error is negligible.

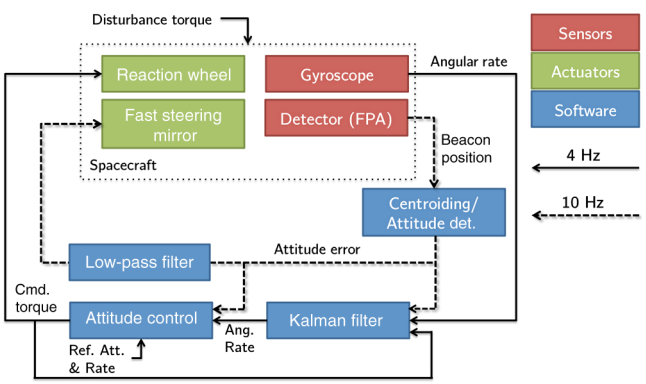

Fig. 4 Block diagram of tracking simulation. Figure originally from Ref. 28.

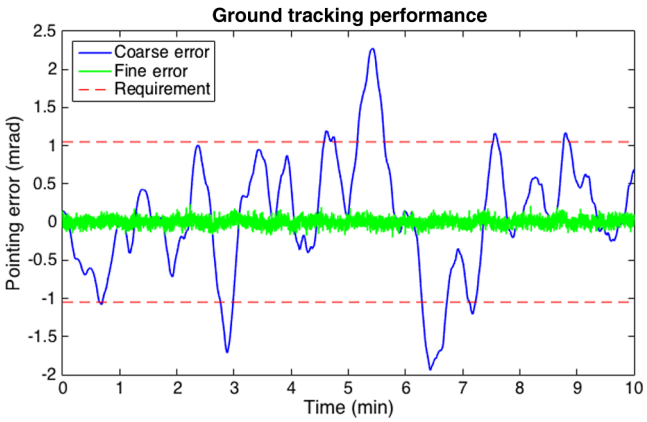

Fig. 5 Coarse and fine stage pointing error with beacon feedback and compensation for environmental disturbances, from Ref. 28.

While only the pitch axis of the satellite is explicitly tracked in the single-axis simulation, environmental disturbances from a six degree of freedom (DOF) simulation are incorporated into the single-axis simulation. The pitch maneuver is modeled in the six-DOF simulation to generate a timeseries of environmental disturbances that include atmospheric drag, gravity gradient, solar radiation pressure, and magnetic disturbances.

3.2.1 *Spacecraft pointing analysis results*

Simulation results indicate that with the addition of an FSM, pointing improves by an order of magnitude. The environmental disturbance torques place significant strain on the host attitude determination and control system, even with estimation and compensation of disturbances. Disturbance torques are generated from the six-DOF simulation while executing ground track maneuvers. The pointing performance of the coarse and fine stages is shown in Fig. 5 and summarized in Table 5. With estimation and compensation for environmental disturbances, the coarse stage can achieve 0.82 mrad RMS, and the fine stage can achieve 0.06 mrad RMS with no Tx/Rx misalignment. When incorporating the calibration analysis, we can calibrate the effects of misalignment to a pointing error of 0.11 mrad, giving a combined pointing error of ~0.3 mrad.

4 Moving Toward a Flight Experiment: Hardware and Firmware Development

In this section, we describe the hardware, software, and control algorithm design and testing. Initial concept development and prototyping has been described in Refs. 22, 23, and 24. Here we extend this work to include descriptions of further design iterations and prototyping efforts. Building on the work of Kingsbury,[22] the team has made progress in the areas of link analysis, circuit board prototyping, mechanical design, modulation, coding and interleaving, design and hardware in the loop control testing of the ground station, and space-qualifying of hardware. In Sec. 4.1, we describe the design and test approaches and results for the NODE transmitter module. In Sec. 4.2, we describe the design and testing of an AT lasercom ground terminal. In Sec. 4.3, we describe the NODE waveform, coding, and interleaving approach.

Table 5 Simulation results of tracking performance of fine and coarse stages.

	RMS error	3σ error
Coarse stage with beacon tracking	0.82 mrad	2.32 mrad
Fine stage with beacon tracking	0.060 mrad	0.18 mrad
Calibration bias	0.11 mrad	0.11 mrad
Combined with modeled misalignment		0.3 mrad

Table 6 Summary of FSM thermal testing and sources of pointing error.

Error source	Worst-case magnitude (mrad)
Thermally induced deformation	<0.15[a]
Zero position repeatability	0.02
Thermal sensitivity shift	0.15[b]
Tip/tilt command repeatability	0.06
Total error	0.38

[a]Further characterization required.
[b]With no compensation in software.

4.1 *Transmitter*

The NODE system uses a MOPA transmitter architecture for scalability, as described in Ref. 22, and a bistatic transmitter/beacon receiver configuration as a result of the constraints on the available volume from the host spacecraft. The trade between a MOPA architecture and a high power laser diode is described further in Ref. 22. We assume the host has a payload that can be coaligned with the transmit aperture toward Earth for closed-loop beacon tracking. A block diagram of the transmitter architecture is shown in Fig. 6. The power distribution unit and field-programmable gate array (FPGA) from the host spacecraft provide power to both the EDFA and FSM Driver Board, as well as other active components. The host FPGA will provide power to a separate NODE break-out board containing a comparator, an amplifier, and resistance temperature detectors (RTDs) for the TOSA. From the TOSA, optical fiber will carry the signal through a circulator directing the optical signal to two paths: a fiber Bragg grating (FBG) filter and a 99:1 coupler. The FBG reflects the optical signal of the desired frequency (frequency of the TOSA) back to the circulator, to continue to the EDFA via a coupler. Photodetectors (PDs) and 99:1 couplers are used for built-in self-test capability for verification of frequency and power output. The EDFA amplifies the signal, and a collimator narrows the beam to 2.26 mrad. The FSM is used to steer the optical beam, which exits via the transmit aperture. Components that dissipate a significant amount of heat in the system (EDFA and TOSA) have been placed in locations that are further from the locations of components requiring a high level of alignment (Collimator and FSM). While performance simulation results using lab-acquired thermal data indicate the NODE

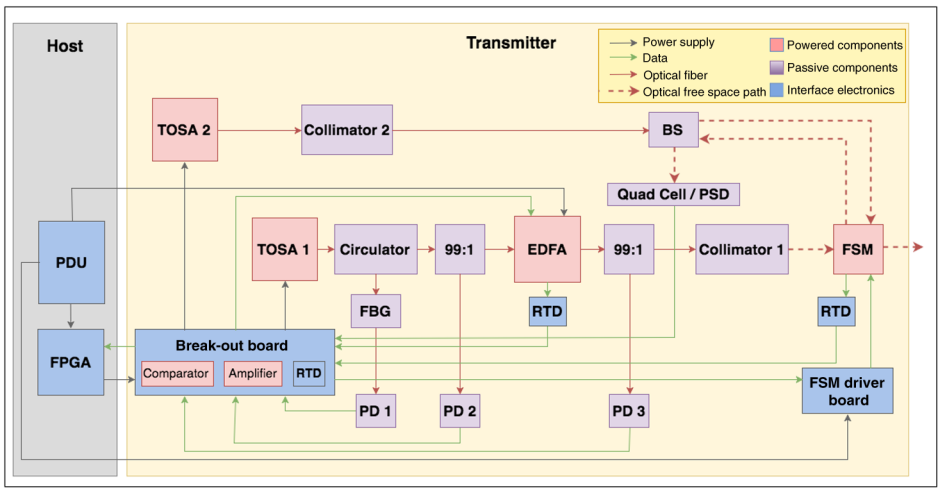

Fig. 6 Block diagram of NODE transmitter architecture.

FSM is expected to meet its performance requirements with open-loop control on its position using a temperature-based lookup table,[22,28] it is possible that additional uncertainties (from changes during the launch environment and alignment, thermal variability, and structural disturbances) could arise. A FSM feedback system consisting of a low-power laser diode and PD will be placed on-board to verify performance of the mirror, as shown in Fig. 6.

After the prototype validation performed in Ref. 22, development of the NODE spacecraft transmitter has centered on adapting it to fit within the severely constrained SWaP of the host spacecraft. This includes designing miniature electronics interface and driver boards, compact mechanical housing assemblies, and refining simulations of the modulation, coding, and interleaving toward flight firmware and software. Additional environmental and radiation tests and analyses are also underway.

4.1.1 *Transmitter electronics*

Work is currently underway on implementing the transmitter design into a low-SWaP package suitable for flight on a CubeSat. Three boards are in development for NODE: (i) the "Breakout Board," carrying the laser control electronics, several resistance temperature detector (RTD) controllers for use in monitoring the temperature of various transmitter components, as well as a Texas Instruments MSP430 microcontroller to assist in interfacing with the host spacecraft, (ii) the driver electronics board for the FSM, which must maintain a steering resolution of 0.01 mrad and supply a drive voltage as high as 160 V, and (iii) and a printed circuit board (PCB)-mounted FSM. Prototypes of these boards can be seen in Fig. 9. Because of the low power and frequency and the shielded inductors used in the design, electromagnetic interference is not a concern. Prototyping of the boards has so far included basic verification with an oscilloscope.

A hardware-in-the-loop experimental setup was constructed in order to validate the performance of the MOPA transmitter, as shown in Fig. 7. The temperature and current of the TOSA board containing the seed laser are controlled by an ILX lightwave laser diode controller, and the laser diode is directly modulated by a Xilinx Spartan 6 FPGA. The output of the seed laser diode is filtered by the FBG circulator and the signal is then amplified by the EDFA before being received by an APD. Power levels are measured at the outputs of the laser diode, the FBG filter, and at the receiver in order to monitor and analyze the performance of the experimental setup.

4.1.2 *Transmitter mechanical design*

The transmitter module mechanical design is composed of two "trays" that are positioned on top of each other and fastened together. While the fiber racetrack tray is similar to the Aerospace OCSD mechanical design,[35,34] NODE requires a second tray for the additional components. The mechanical layout is constrained by the bending radius and splice locations of the fiber that connect the components. The bottom tray houses and secures components such as the miniature electronics boards, lasers, and filters in cutouts with adhesive. The top tray is a "racetrack" in which the fiber wraps around restraints to maximize the bend radius and minimize losses, and extra fiber is accommodated.[76] Figure 8 shows an initial CAD rendering of both trays with included components. A fit check with an early design revision is shown in Fig. 9.

Because of the complex geometries required for mounting components in the SWAP-constrained system, additive manufacturing techniques[77] may be required as the design evolves, but the current design necessitates only traditional techniques.

Critical components and assemblies will undergo thermal testing to verify alignment at all temperature ranges, and thermal testing has already begun for the FSM, which has been found to perform consistently in the expected temperature range during initial thermal cycling in an air oven. Kingsbury[22] and Riesing[28] showed that the FSM is able to maintain the required accuracy for all expected temperatures, as shown in Table 6. The testbed developed for measuring FSM response and the thermal chamber used for environmental showed that the primary sources of FSM error are device hysteresis and thermal sensitivity.[28] While mitigation strategies exist, including obtaining position feedback from the mirror, even without implementing the mitigations, the inclusion of the additional errors on the FSM measured during test into the pointing and tracking simulation results in overall pointing error of 0.38 mrad in the worst case, which is still within the pointing budget of 1.05 mrad.

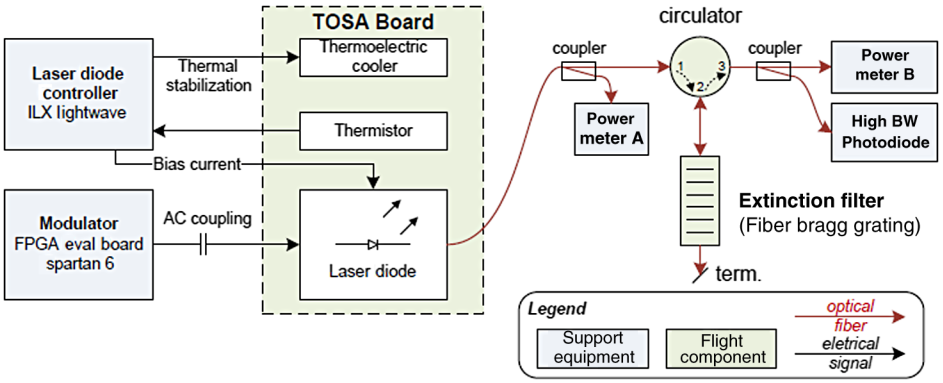

Fig. 7 Experimental configuration for transmitter alignment with FBG filter for measuring output signal extinction ratio.[22]

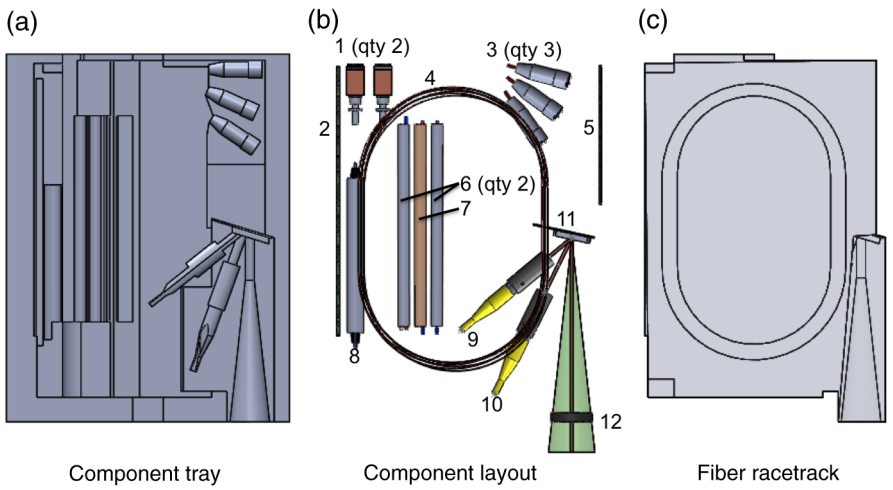

Fig. 8 Initial CAD drawing of NODE transmitter tray module. (a) The component tray, (b) the component layout, and (c) the racetrack that holds the fiber loops is a work in progress. The components are numbered as follows: 1. TOSAs, 2. Breakout board, 3. PDs, 4. Fiber, 5. Driver Board, 6. Optical couplers, 7. FBG, 8. Circulator, 9. Signal collimator, 10. Feedback collimator, 11. FSM, 12. Transmitter aperture.

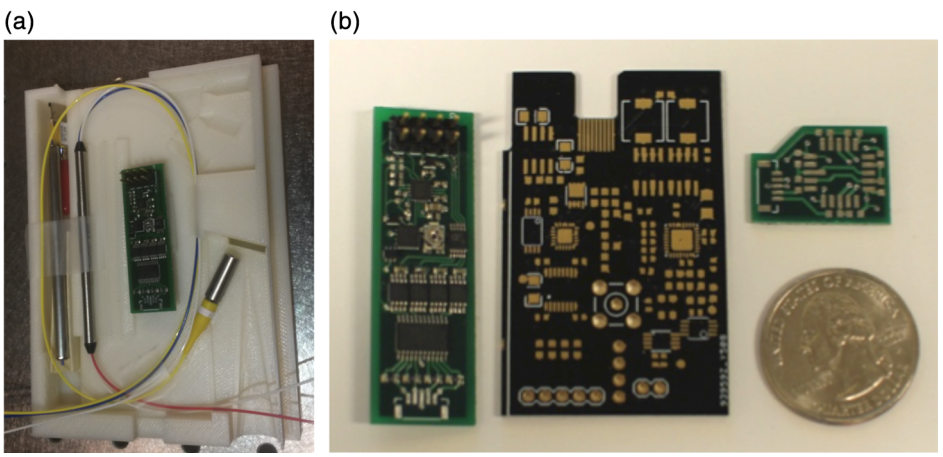

Fig. 9 Prototype hardware of transmitter housing and electronics. (a) is a fit check of key components in three-dimensional-printed structure. Jacketed fiber is shown to highlight the fiber routing. Couplers and a FBG fit into long slots, and the collimator fits into the short slot in bottom center. The FSM will fit in the deep slot opposite the collimator. Placement of other components, such as the mirror driver board shown in the center, is in revision as a result of this fit check. (b) shows the FSM driver board (left), unpopulated breakout board prototype (center), and FSM mounting PCB (top right).

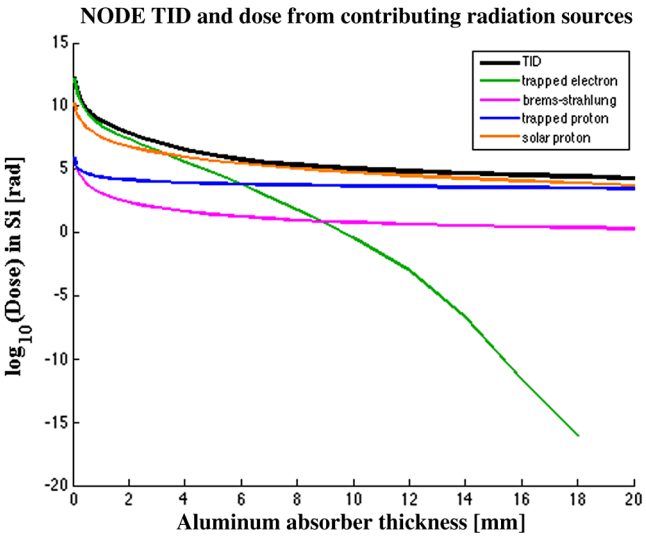

Fig. 10 NODE total ionizing dose and dose from contributing radiation sources. The mission was modeled with SPENVIS for a 475-km sun-synchronous orbit and 1-year mission duration starting on March 1, 2017. Trapped particle models AE8-MAX and AP9-MIN, long-term solar particle fluence model ESP-PSYCHIC, GCR flux model ISO 15390, and ionizing dose model SHIELDOSE-2 were the models used to calculate the expected TID for the mission.

4.1.3 *Transmitter radiation assessment*

We conducted a radiation analysis for the mission using the European Space Agency's space environment information System, SPENVIS. As a LEO mission, NODE will be exposed to radiation from particles trapped by Earth's magnetic field, from solar particle events (SPEs), and from galactic cosmic rays (GCR).[78] The expected total ionizing dose (TID) as well as dose from trapped protons, trapped electrons, SPEs, and GCRs for various aluminum shielding thicknesses are displayed in Fig. 10. The chassis walls for the host spacecraft have a thickness between 1.0 and 5.0 mm, and from the SPENVIS results, aluminum shielding of these thicknesses will yield an expected TID level between 6.795 and 0.456 krad over the 1 year mission. While testing of similar electrical components has shown sensitivity to radiation effects,[79,80] the board with the most sensitive components will have sufficient shielding to protect against high dose levels for the expected particle energy levels. Studies of the radiation effects on optical components, such as PDs,[81] the FBG filter,[82] and EDFA,[83] have suggested that radiation does not significantly affect the performance of these components for typical radiation levels. Therefore the shielding provided by the chassis walls of the host spacecraft and the transmitter trays is likely to mitigate radiation effects of the trapped particle environment.

4.2 *Ground Station*

The ground station uses an AT (currently a Celestron CPC 1100) as the main aperture to collect the laser signal (the electronics are also designed to be compatible with OCTL as another possible ground station). A COTS APD converts the light into an electronic signal that is processed and delivered as the data output, and infrared camera is used to aid in pointing and tracking of the telescope. Figure 11 shows the optical layout of the receiver. Table 7 contains the design parameters for the key ground station components. The limiting factor on this design is the field-of-view (FoV) of the APD sensor, due to the small size of the PD (just 200 μm).

We are developing a postprocessing receiver for NODE due to time and resource constraints. The receiver electronics will be modeled after the Lunar Laser OCTL Terminal (LLOT) employed by JPL during the LLCD.[84] The receiver will sample the electrical signal from the APD using a 3.6-GS/s ultra wideband RF/IF portable recorder, employing a 12-bit A/D converter to provide a maximum sampling rate of 3.6 GS/s in single channel mode. It may record data at up to 4.8 GB/s and has 15.3 TB of solid state drive storage in a new technology file system redundant array of independent disks solid state disk array. In order to accurately reconstruct the signal digitally, Nyquist requires >400 MS/s sampling due to our 200 MHz slot rate, and the recorder gives us the ability to oversample the signal at rates ≥800 MS/s in order to more reliably demonstrate performance and test our clock recovery algorithms. While we have not yet performed signal-to-quantization-noise ratio calculations to determine the minimum number of bits per sample needed, we expect that the 12-bit A/D will be more than sufficient for our purposes since the LLOT used an 8-bit A/D successfully. After successfully sampling the waveform, the clock recovery algorithms, digital demodulator, deinterleaver, and decoder will recover the data. Figure 13 shows the functions of the postprocessing receiver.

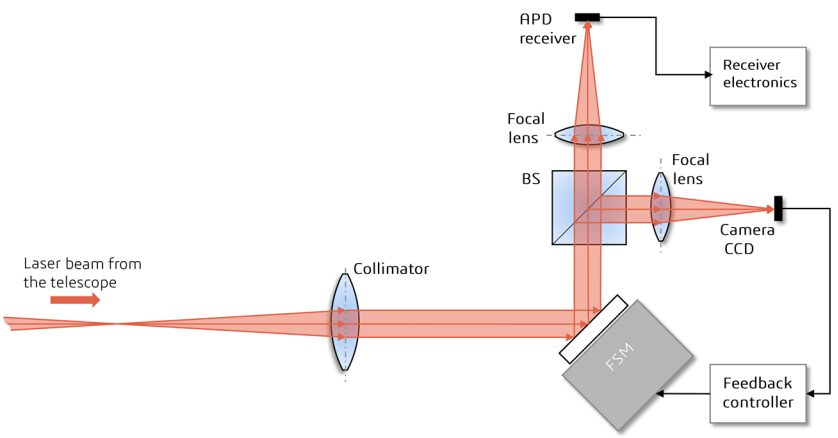

Fig. 11 Ground station optical system layout. Light from the amateur astronomy-class telescope enters on the left.

Table 7 Ground station design parameters. The FoV of the APD and the tracking camera is given by the focal lengths of the telescope, collimator, and focal lenses, as well as by the size of the APD and the CCD sensor, respectively.

Measure	Value	Units
Signal spot size	13.5	μrad
APD FoV	119.1	μrad
Tracking camera FoV	2.44×1.92	mrad
Initial pointing error (1 km error, 800 km range)	1.26	mrad
FSM accuracy required (mechanical)	0.01	mrad
FSM range to cover camera FoV (mechanical)	± 33.3	mrad
FSM minimum size to cover camera FoV	11.7×10.3	mm

The ground station pointing system consists of two stages: (i) the telescope control for satellite tracking and (ii) the FSM for fine pointing. The telescope provides coarse pointing of the tracking camera using the COTS telescope mount which has Azi-Alt gimbals. Custom tracking software uses the simplified general perturbations 4 (SGP4) orbit propagator[85] and an Earth model from the International Earth Rotation and Reference Systems Service (IERS).[86] It is expected to provide the orbit determination error to less than 1 km, or the pointing vector estimation error to less than 0.06 deg for 1000-km range. With good knowledge of the telescope alignment with respect to a reference frame such as J2000 or the earth-centered-earth-fixed (ECEF) frame, it is possible to track the satellite within the FoV of the iNova PLB-Mx2 star tracking camera, an astronomy camera. (While amateur astronomers use the built-in telescope alignment capability for pointing the telescope to a known star manually, this method is not suitable for our application because the alignment accuracy is not repeatably quantifiable and it highly depends on the user ability.[87]) The camera FoV is wide enough to take an image of star patterns of multiple stars as shown in Fig. 12. With multiple measurements from different parts of the sky, we can calculate the alignment of the telescope with respect to ECEF frame as well as the alignment of the star camera frame to the telescope mount. By comparing the star positions on the captured image and the expected star positions calculated from a star catalog, we can quantify the star camera's accuracy as well as the pointing error. In our initial attempts with the closed loop approach, we have been able to image a star with an Orion camera and record the video. With a feedback loop using the star camera, we demonstrated a tracking error of about 60 arc sec or 0.3 mrad, which is smaller than the narrow FoV of the tracking camera. We expect that the residual error will be reduced to within the APD's FoV when we add the fine pointing feedback loop of the tracking camera and FSM.

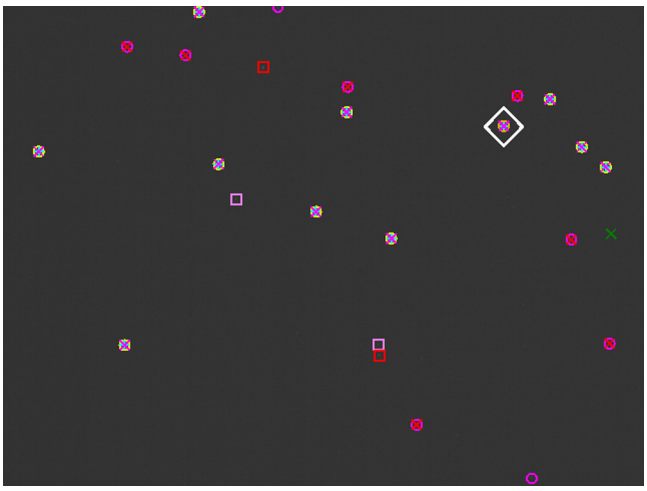

Fig. 12 Identified star pattern image whose FoV is 7.8 deg $\times$ 5.9 deg. circle markers, captured stars; crosses, stars from a star catalog. We identify the stars in the star pattern image using a correlation-based star identification algorithm[88,89] and calculate the attitude quaternion of the camera frame from the captured stars' positions on the image and their positions from a star catalog in an inertial frame such as J2000.

4.3 *Waveform, Coding, and Interleaving*

NODE uses M-ary PPM (M-PPM) to encode the data and modulate the laser. PPM was chosen as the modulation format for NODE because we are using an average-power-limited EDFA implementation for low-cost COTS-based CubeSat lasercom, although other design approaches, such as coherent detection, may have advantages. The waveform selected for NODE may not be optimal for all cases. NODE nominal operations use 16-PPM, 32-PPM, 64-PPM, and 128-PPM. With the fixed slot width, the adjustable PPM order allows the data rate to change. Larger PPM orders result in larger peak power, and this larger peak power results in an increased SNR at the receiver. For this reason, larger PPM orders result in larger received SNR but lower data rates, and the inverse is true for low PPM orders. NODE will use an intersymbol guard "dead" time to prevent back-to-back pulses from hitting the EDFA, which would result in a loss in amplification because the EDFA would not have time to recover. The intersymbol guard time also provides a periodic reference that is helpful for clock recovery.[90] Discussion and detail regarding the selection of PPM can be found Ref. 22.

NODE will use Reed–Solomon (RS) encoding, interleaving, and Gray coding to overcome the channel impairments. We chose to use RS as the error-correcting code since it is a strong error-correcting code and has many open-source implementations. Since the physical layer for NODE was designed to provide a 1×10^{-4} BER, an RS (255,239) code is sufficient to provide near error-free performance.[22,72,91,92] Full system tests may indicate that a lower rate code should be used, and the codec for NODE may be set to a different rate in software before launch. However, once on orbit, the code rate will be fixed.

It has been shown that the optical channel from LEO to ground is characterized by long fades on the order of milliseconds that result in burst errors for the data.[22,72,93,94] These burst errors cause multiple correlated errors in one codeword, and the fades are long enough such that the number of errors in one codeword will exceed the error correcting capabilities of the code. Linear block codes, such as RS codes, do not perform well in the presence of burst errors because entire codewords may be lost.[22] Interleavers have been shown to effectively combat the negative effects caused by channel

fades when paired with forward error correction, and for this reason, NODE will use a block interleaver.[22,72,93,94] We chose a fade depth of 1 s since a common design practice for interleavers is to have the depth of the interleaver be 100 to 1000 times the coherence time of the channel fading process, which, as stated earlier, is on the order of milliseconds.

Since NODE will use PPM orders of 16, 32, 64, and 128, the modulator will encode 4, 5, 6, and 7 bits per PPM symbol, respectively. The RS(255,239) code uses 8 bits per RS symbol. This poses a problem as two PPM symbols span each RS symbol for PPM orders of 32, 64, and 128. If either PPM symbol is received in error, the codeword will be received in error, and with two PPM symbols spanning each RS symbol, one PPM symbol error could cause two RS symbols to be received in error. This would result in more errors per RS codeword than expected. To reduce the amount of bit errors caused by this occurrence, NODE will use Gray coding on the encoded and interleaved data stream before it is passed into the modulator. In the presence of nonoptimal receiver synchronization, symbol errors may occur when the receiver erroneously decides that a slot adjacent to the transmitted slot was sent, and Gray coding will ensure the symbols corresponding to adjacent slots are mapped into bit patterns that differ by only one bit. In this way, the number of RS symbol errors may be minimized for NODE so that there is a lesser chance that the RS(255,239) code is pushed beyond its error-correcting capabilities.

4.3.1 *Waveform, coding, interleaving firmware development*

The block diagram in Fig. 13 gives an overview of the waveform design and receiver electronics as presented in Sec. 4.3. Results obtained from our MATLAB® simulations confirm that, given an uncoded BER of 10^{-4}, the RS(255,239) code will provide a coded BER of 10^{-18}, which we deem to be error-free. Additionally, MATLAB® and Python simulations show that burst errors are corrected when pairing a simple block interleaver with the RS(255,239) code. The MATLAB® simulation includes a model of the atmospheric channel, and the atmospheric channel accounts for the effects of absorption and scatter, scintillation, shot noise, and thermal noise. Figure 14 generated from the MATLAB® simulation shows how we expect the optical channel to affect the waveform.

For a transmitter using 32-PPM and limited to 0.2 W average optical output power, Fig. 14 shows what we expect the waveform to look like after passing through the optical channel. The simulations show that NODE can obtain error-free performance while using the channel model when using M-PPM, RS(255,239), and a block interleaver. The simulation is currently being adjusted so that the channel model adds timing errors that will occur due to oscillator drift and Doppler. Additionally, since NODE will employ a post-processing receiver, clock recovery will occur digitally in software, and clock recovery algorithms are being developed in MATLAB®. The receiver must determine the slot clock and symbol clock from the PPM waveform in order to recover the data, where the slot clock determines the slot boundaries while the symbol clock determines the symbol boundaries.[90,95,96–98] We are developing a digital early-late gate to recover the slot clock.[95,99] The intersymbol guard times inserted at the transmitter help in recovering the symbol clock once the slot clock has been obtained. A correlation across the dead times and choosing the minimum correlation will reveal the symbol clock.[90]

Upon obtaining the slot clock and symbol clock, demodulation will be performed to correctly recover the data. Framing will be employed on the FPGA to provide an acquisition sequence and idle fill; and we consider this framing to be physical layer framing. The acquisition sequence will provide good correlation features, much like the acquisition sequence used in LLCD.[99] NODE's acquisition sequence will employ a multitude of PPM orders in order to give it good correlation features. The acquisition sequence will aid in initial clock recovery. The idle fill will provide a means to keep data flowing into the modulator when the first in first out on the FPGA is empty or the data path to the FPGA experiences delays. NODE will use 1 s frames, much like those used in Ref. 100; however, we will not need to insert synchronization symbols since we use intersymbol guard times. We will not use a spatial acquisition sequence as our transmitter will have a tracking mode, and our acquisition sequence will serve the same purpose as

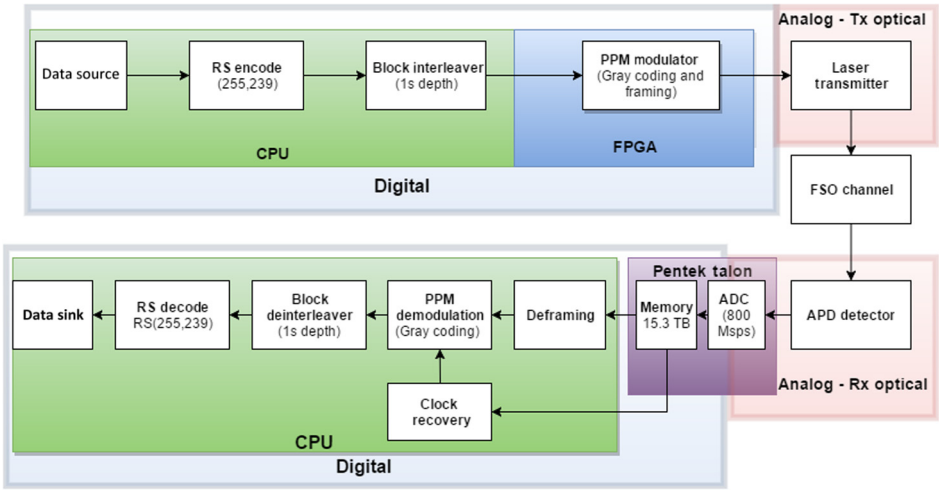

Fig. 13 NODE waveform block diagram: waveform, coding, interleaving, and receiver electronics.

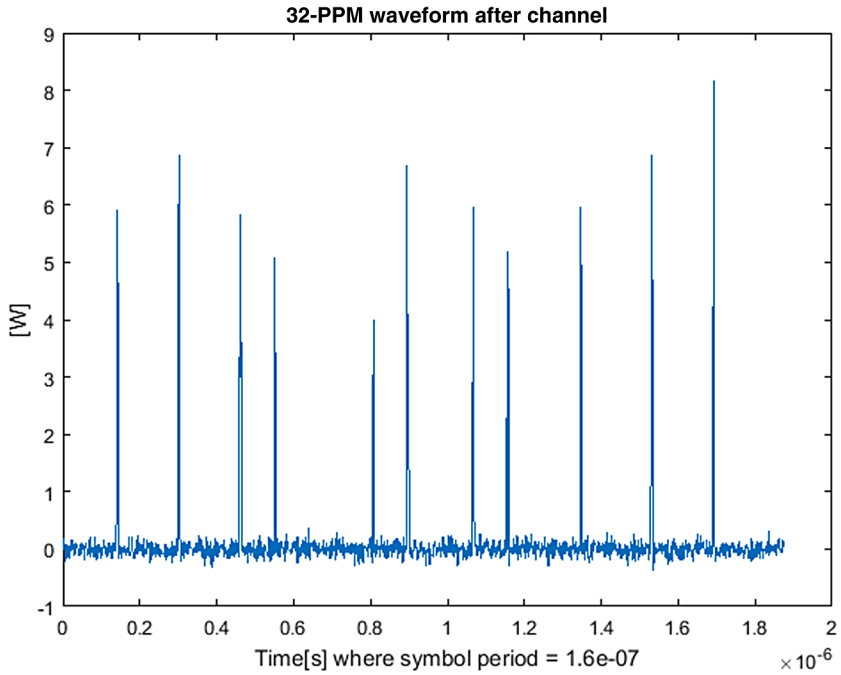

Fig. 14 PPM waveform after being passed through channel model. For simplicity, the channel model does not include the attenuation expected due to free-space path loss, meaning the amplitude is not what we expect the receiver to see. However, we expect the received signal to be a scaled version of the signal.

the frame sync pattern in Ref. 100. One-second frames were chosen as they work well with the 1-s interleaver, meaning we do not have to interleave over multiple frames.

5 Summary and Future Work

The goal of NODE is to demonstrate a rate-scalable, low-SWaP, low-cost laser communications downlink from a CubeSat. In the initial demonstration, the objective is to achieve downlink rates better than 10 Mbps to a 30-cm ground station aperture with 0.2 W transmit power as a pathfinder toward even higher-rate, low-cost CubeSat lasercom systems. This will enable future CubeSat missions with power-limited and downlink-limited payloads to run the payloads and downlink at higher duty cycles.

In this paper, we summarized and extended the work of Kingsbury[22] and reported findings from both simulation and prototyping. We described a probabilistic approach to lasercom link budgets that uses uncertainty analysis and sensitivity analysis to guide design and testing, and found that with a modest initial demonstration beamwidth of 2.26 mrad, we expect greater than 90% probability of positive margin for a 10-Mbps link to the 30-cm AT at 1000-km range and for a 43-Mbps link to the 1-m OCTL ground station under moderate atmospheric conditions. Electronics prototyping includes the thermoelectric cooler (TEC) control electronics and mirror driver, and ongoing TEC software development and calibration. Mechanical development includes a concept for housing that uses additive manufacturing, component-level thermal testing to work toward space-qualifying the COTS transmitter components, and radiation analysis that indicates radiation is not a major concern for this initial short demonstration. The approach to use an RS(255,239) code applied after Gray coding (to reduce the chance that a PPM symbol could cross RS blocks) was described in detail, along with the rationale for a 1-s block interleaver depth. A MATLAB® simulation was developed that demonstrated error-free communications with these constraints. Simulations of coarse and fine stage pointing error combined with an analysis of misalignment predict pointing error of ± 0.3 mrad 3-σ, well within the ± 1.05 mrad requirement. Analysis of the two-stage approach to the ground station and receive APD for the AT identified 119.1 mrad as the ground station pointing requirement. Testing of a new star-tracking alignment approach demonstrated that the current ground station telescope coarse stage can achieve about 60 arc sec pointing error (about 0.3 mrad). This will inform selection of the second stage, and FSM, which will achieve the requirement.

While this paper describes the development of an initial onorbit NODE demonstration, future systems may build on the work of NODE to improve the data rate. While future CubeSats will still be power-limited, the data rate can increase by improving component performance, such as higher quality transmitter components that allow more diverse slot widths, incorporating WDM, and improving the pointing capability.

Acknowledgments

The authors appreciate the contributions and feedback from several collaborators, most notably Ryan Kingsbury, who developed the NODE system concept for his dissertation, and who spearheaded the prototyping and testing of the transmitter module. We also acknowledge mentorship from Jeff Mendenhall, Michael Shatz, Don Boroson, Brian Wolf, Fred Block, Thomas Royster, Ryan Shoup, and Matthew Johnson from MIT Lincoln Laboratory, Bill Farr from NASA JPL, and Ron Logan from Glenair. The NODE project has been supported by the MIT Deshpande Program

and a JPL SURP grant. Ryan Kingsbury and Kathleen Riesing have been supported by the NASA Space Technology Research Fellowship program, Emily Clements by the MIT Lincoln Laboratory Lincoln Scholars and Caleb Ziegler by the Military Fellowship program, Iñigo del Portillo by an Obra Social La Caixa Fellowship, and Hyosang Yoon by a Samsung Fellowship. The Lincoln Laboratory portion of this work is sponsored by the Assistant Secretary of Defense for Research & Engineering under Air Force Contract #FAs872105C0002. Opinions, interpretations, conclusions, and recommendations are those of the author and are not necessarily endorsed by the US Government. The views expressed in this article are those of the author(s) and do not reflect the official policy or position of the US Air Force, Department of Defense, or the US Government.

References

1. M. Swartwout, "The first one hundred CubeSats: a statistical look," *J. Small Satell.* **2**(2), 213–233 (2013).
2. M. Swartwout, "Secondary spacecraft in 2015: analyzing success and failure," in *2015 IEEE Aerospace Conf.*, pp. 1–12, IEEE (2015).
3. R. Pournelle and M. Johnson, "NanoRacks CubeSat deployment services," in *Small Satellite Conf.*, Logan, Utah, Paper SSC14-WK-25 (2014).
4. W. Blackwell et al., "Nanosatellites for earth environmental monitoring: the MicroMAS project," in *2012 IEEE Int. Geoscience and Remote Sensing Symp. (IGARSS)*, 206–209, IEEE (2012).
5. H. Smith, S. Hu, and J. Cockrell, "NASA's EDSN aims to overcome the operational challenges of CubeSat constellations and demonstrate an economical swarm of 8 CubeSats useful for space science investigations," in *AIAA/USU Small Satellite Conf.*, Logan, Utah, Paper SSC-XI-2 (2013).
6. B. Klofas, "CubeSat communication systems table, version 10," http://www.klofas.com/comm-table/ (14 April 2016).
7. E. Buchen and D. DePasquale, "2014 Nano/Microsatellite Market Assessment," *SpaceWorks Enterprises*, 2014, Inc.(SEI) Atlanta, Georgia, http://www.sei.aero/eng/papers/uploads/archive/SpaceWorks_Nano_Microsatellite_Market_Assessment_January_2014.pdf (29 August 2015).
8. B. Klofas and K. Leveque, "The future of CubeSat communications: transitioning away from amateur radio frequencies for high-speed downlinks," in *AMSAT-NA Space Symp.*, Orlando, Florida (2012).
9. D. Selva and D. Krejci, "A survey and assessment of the capabilities of CubeSats for earth observation," *Acta Astronaut.* **74**, 50–68 (2012).
10. S. Tsitas and J. Kingston, "6U CubeSat design for Earth observation with 6.5 m GSD, five spectral bands and 14Mbps downlink," *Aeronaut. J.* **114**(1161), 689–697 (2010).
11. J. Bouwmeester and J. Guo, "Survey of worldwide pico- and nanosatellite missions, distributions and subsystem technology," *Acta Astronaut.* **67**(7), 854–862 (2010).
12. B. Klofas and K. Leveque, "A survey of CubeSat communication systems: 2009–2012," in *10th Annual CubeSat Developers Workshop*, Cal Poly State University, San Luis Obispo, California (2013).
13. J. A. King et al., "Ka-band transmitter status," in *29th Annual AIAA USU Conf. on Small Satellites Small Satellite Communications Workshop* (2015).
14. B. Cooper, "Spacecraft manufacturing: lessons learned from Corvus-BC," in *2016 CubeSat Developers Workshop* (2016), http://polyplayback.ceng.calpoly.edu/Mediasite/Catalog/catalogs/cubesat-developers-workshop-spring-2016
15. Tethers Unlimited, "SWIFT-XTS/SFN," http://www.tethers.com/SpecSheets/Brochure_SWIFT_XTS_SFN.pdf
16. A. D. Marinan, "From CubeSats to constellations: systems design and performance analysis," PhD Thesis, Massachusetts Institute of Technology (2013).
17. Tethers Unlimited, "SWIFT-SLX,"http://www.tethers.com/SpecSheets/Brochure_SWIFT_SLX.pdf
18. D. Mandl et al., *Hyperspectral CubeSat Constellation for Rapid Natural Hazard Response* (2015).
19. M. Long et al., "A CubeSat derived design for a unique academic research mission in earthquake signature detection," in *Proc. AIAA Small Satellite Conf.* (2002).
20. "NanoCam C1U," http://www.cubesatshop.com/index.php?page=shop.product_details&flypage=flypage.tpl&product_id=63&category_id=16&option=com_virtuemart&Itemid=80
21. "Hyperspec VNIR imaging sensors for the 380–1000 nm spectral range," http://cdn2.hubspot.net/hubfs/145999/docs/VNIR.pdf?t=1459861981807 (February 2016).
22. R. W. Kingsbury, "Optical communications for small satellites," PhD Thesis, Massachusetts Institute of Technology (2015).
23. R. Kingsbury, D. Caplan, and K. Cahoy, "Compact optical transmitters for CubeSat free-space optical communications," *Proc. SPIE* **9354**, 93540S (2015).
24. R. Kingsbury, D. Caplan, and K. Cahoy, "Implementation and validation of a CubeSat laser transmitter," *Proc. SPIE* **9739**, 973905 (2016).
25. T. Nguyen et al., "Development of a pointing, acquisition, and tracking system for a CubeSat optical communication module," *Proc. SPIE* **9354**, 93540O (2015).
26. R. Kingsbury, K. Riesing, and K. Cahoy, "Design of a free-space optical communication module for small satellites," in *Small Satellite Conf. Proc.* (2014).
27. R. Kingsbury et al., "Fast-steering solutions for CubeSat-scale optical communication," in *Proc. of Int. Conf. on Space Optics* (2014).
28. K. M. Riesing, "Development of a pointing, acquisition, and tracking system for a nanosatellite laser communications module," Master's Thesis, Massachusetts Institute of Technology (2015).
29. D. M. Boroson et al., "Overview and results of the lunar laser communication demonstration," *Proc. SPIE* **8971**, 89710S (2014).
30. T. Jono et al., "OICETS on-orbit laser communication experiments," *Proc. SPIE* **6105**, 610503 (2006).
31. B. L. Edwards et al., "Overview of the laser communications relay demonstration project," in *Proc. of SpaceOps*, p. 1261897 (2012).
32. A. Biswas, "Space technology mission directorate game changing development program deep space optical communications (DSOC)," https://evt.grc.nasa.gov/rfp-industry-briefing-2016/wp-content/blogs.dir/52/files/sites/10/Deep-Space-Optical-Communications-DSOC-Overview.pdf (6 January 2016).
33. H. Takenaka et al., "In-orbit verification of small optical transponder (SOTA): evaluation of satellite-to-ground laser communication links," *Proc. SPIE* **9739**, 973903 (2016).
34. T. S. Rose et al., "Leo to ground optical communications from a small satellite platform," *Proc. SPIE* **9354**, 93540I (2015).
35. R. P. Welle et al., "CubeSat-scale laser communications," in *31st Space Symp.*, Colorado Springs (2015).
36. P. Serra, N. Barnwell, and J. W. Conklin, "A novel, low power optical communication instrument for small satellites," in *Small Satellite Conf.*, Paper SSC15-VI-10 (2015).
37. "1u CubeSat lasercom terminal for deep space communication," https://www.sbir.gov/sbirsearch/detail/702459 (2014).
38. "1u CubeSat lasercom terminal for deep space communication," https://www.sbir.gov/sbirsearch/detail/888145 (2015).
39. D. Messier, "NASA selects small business CubeSat projects for funding," http://www.parabolicarc.com/2015/04/26/digital-solid-state-propulsion/ (26 April 2015).
40. J. Kovalik, W. Farr, and S. Piazzolla, "Laser communications subsystem for interplanetary CubeSats," Poster at ISSC (2015).
41. C. Henry, "Bridgesat plans optical netowrk for smallsats, UAVs," http://www.satellitetoday.com/technology/2015/10/02/bridgesat-plans-optical-network-for-smallsats-uavs/ (2 October 2015).
42. Allied Minds, "Surrey satellite and BridgeSat to develop free space satellite optical communications solution," http://www.alliedminds.com/announcements/surrey-satellite-and-bridgesat-to-develop-free-space-satellite-optical-communications-solution.
43. M. Albert, "Long range optical telecommunications," (2016). http://sbir.gsfc.nasa.gov/SBIR/abstracts/16/sbir/phase1/SBIR-16-1-H9.01-8407.html.
44. G. Yang et al., "Innovative free space optical communication and navigation system with high data rate communication, precision ranging, range rate measurements, and accurate spacecraft pointing," *Proc. SPIE* **9739**, 97390K (2016).
45. Prof. Brian Gunter: hitching a ride with Google, skybox, http://www.ae.gatech.edu/node/1945 (20 December 2015).
46. J. Conklin et al., "Optical time transfer for future disaggregated small satellite navigation systems," (2014).
47. B. A. Cohen et al., "Lunar flashlight: mapping lunar surface volatiles using a CubeSat," in *Annual Meeting of the Lunar Exploration Analysis Group*, Vol. **35812**, p. 3031 (2014).
48. R. Fields et al., "A linear mode photon-counting (LMPC) detector array in a CubeSat to enable earth science lidar measurements," in *2015 IEEE Int. Geoscience and Remote Sensing Symp. (IGARSS)*, pp. 5312–5315, IEEE (2015).
49. D. Gershgorn, "Facebook will use these lasers to beam internet from the sky," http://www.popsci.com/facebook-will-use-these-lasers-beam-internet-sky (2 July 2015).
50. P. De Selding, "Thales Alenia Space wins initial funding for high-altitude platform, plans 2018 demo," SpaceNews, http://spacenews.com/thales-alenia-space-high-altitude-platform-wins-initial-funding-plans-2018-demonstration/#sthash.yyiCEc6k.dpuf (26 April 2016).
51. M. Gidda, "Google and Facebook plan to reach remote areas of the planet." http://europe.newsweek.com/google-facebooks-plan-reach-remote-areas-planet-336160 (11 July 2015).
52. C. Metz, "Google laser-beams the film real genius 60 miles between balloons." http://www.wired.com/2016/02/google-shot-laser-60-miles-just-send-copy-real-genius/ (24 February 2016).

53. "Blue Canyon Technologies XACT datasheet," http://bluecanyontech.com/wp-content/uploads/2016/01/XACT-Data-Sheet_2.0.pdf (January 2016).
54. K. Sarda et al., "Canadian advanced nanospace experiment 2 orbit operations: two years of pushing the nanosatellite performance envelope," in *ESA Small Satellites, Services and Systems Symp.* (2010).
55. S. Arnold et al., "QbX-the CubeSat experiment," in *Small Satellite Conf.*, Paper SSC12-XI-4 (2012).
56. S. Janson et al., "Attitude control on the pico satellite solar cell testbed-2," in *Small Satellite Conf.*, Paper SSC12-II-1 (2012).
57. D. Rowen and R. Dolphus, "3-axis attitude determination and control of the aerocube-4 CubeSats," in *AIAA/USU Conf. on Small Satellites, 10th Annual CubeSat Developers' Workshop* (2013).
58. K. Sarda et al., "On-orbit performance of the bright target explorer (BRITE) nanosatellite astronomy constellation," in *Small Satellite Conf.*, Paper SSC14-XII-6 (2014).
59. J. P. Mason et al., "Miniature x-ray solar spectrometer (MinXSS)-a science-oriented, university 3u CubeSat," *arXiv preprint arXiv:1508.05354* (2015).
60. "Perfect precision for MinXSS CubeSat supplied by Blue Canyon Technologies-it's all about attitude." Satnews Daily, http://satnews.com/story.php?number=31922882 (3 July 2016).
61. G. Bonin et al., "Canx–4 and canx–5 precision formation flight: mission accomplished!" (2015).
62. J. Newman, "Drift recovery and station keeping results for the historic canx-4/canx-5 formation flying mission," (2015).
63. A. Biswas et al., "LLCD operations using the optical communications telescope laboratory (OCTL)," *Proc. SPIE* **8971**, 89710X (2014).
64. D. V. Murphy et al., "LLCD operations using the lunar lasercom ground terminal," *Proc. SPIE* **8971**, 89710V (2014).
65. T. Tolker-Nielsen and G. Oppenhauser, "In-orbit test result of an operational optical intersatellite link between ARTEMIS and SPOT4, SILEX," *Proc. SPIE* **4635**, 1 (2002).
66. A. Saltelli et al., *Global Sensitivity Analysis: the Primer*, John Wiley & Sons (2008).
67. K. D. Stout, "Bayesian-based simulation model validation for spacecraft thermal systems," PhD Thesis, Massachusetts Institute of Technology (2015).
68. B. Moision and H. Xie, "An approximate link equation for the direct-detected optical PPM link," *Interplanet. Netw. Prog. Rep.* **199**(27), 1 (2014).
69. L. C. Andrews and R. L. Phillips, *Laser Beam Propagation through Random Media*, Vol. **1**, SPIE Press, Bellingham, Washington (2005).
70. Celestron, "CPC 1100 GPS (XLT) computerized telescope," http://www.celestron.com/browse-shop/astronomy/telescopes/cpc-1100-gps-(xlt)-computerized-telescope (May 2016).
71. K. Wilson et al., "Preliminary characterization results of the optical communications telescope laboratory telescope," *The Interplanetary Network Progress Report*, **42**, 161 (2005).
72. H. Hemmati, *Near-Earth Laser Communications*, CRC Press (2009).
73. P. W. Nugent, J. A. Shaw, and S. Piazzolla, "Infrared cloud imager development for atmospheric optical communication characterization, and measurements at the JPL table mountain facility," *Interplanet. Netw. Prog. Rep.* **42**(192), 1–31 (2013).
74. R. J. Alliss and B. D. Felton, "Improved climatological characterization of optical turbulence for space optical imaging and communications," in *Advanced Maui Optical and Space Surveillance Technologies Conf.*, p. E25 (2010).
75. Thorlabs Inc., *4.7 mm Focal Length Fiber Pigtail Collimator*, revision c ed., Drawing 17382-E01, Part number CFS5-1550-APC (2010).
76. Ron Logan of Glenair, April 27 (2016).
77. D. Manfredi et al., "Direct metal laser sintering: an additive manufacturing technology ready to produce lightweight structural parts for robotic applications," *La Metallurgia Italiana* (10) (2014).
78. R. Aniceto, W. Lohmeyer, and K. Cahoy, "Total ionizing dose requirements for low earth orbit small satellites. 1999," *J. Small Satell.* (2015) (In Progress).
79. J. Byrne, E. Thompson, and R. Kingsbury, "Space radiation environmental analysis of CubeSat components," (2015).
80. R. Kingsbury et al., "TID tolerance of popular CubeSat components," in *50th Nuclear and Space Radiation Effects Conf.* (2013).
81. E. Clements et al., "Interplanetary space weather effects on lunar reconnaissance orbiter avalanche photodiode performance," (2016).
82. A. Gusarov et al., "High total dose radiation effects on temperature sensing fiber Bragg gratings," *IEEE Photonics Technol. Lett.* **11**(9), 1159–1161 (1999).
83. O. Berné, M. Caussanel, and O. Gilard, "A model for the prediction of EDFA gain in a space radiation environment," *IEEE Photonics Technol. Lett.* **16**(10), 2227–2229 (2004).
84. M. Srinivasan et al., "A post-processing receiver for the lunar laser communications demonstration project," *Proc. SPIE* **8610**, 86100Q (2013).
85. D. Vallado and P. Crawford, "SGP4 orbit determination," in *AIAA/AAS Astrodynamics Specialist Conf. and Exhibit* (2008).
86. G. Petit and B. Luzum, "IERS conventions (2010)," Vol. **179** (2010).
87. H. Yoon, R. Kathleen, and C. Kerri, "Satellite tracking system using amateur telescope and star camera for portable optical ground station," in *Proc. Small Satellite Conf.*, Logan (2016).
88. H. Yoon, Y. Lim, and H. Bang, "New star-pattern identification using a correlation approach for spacecraft attitude determination," *J. Spacecr. Rockets* **48**(1), 182–186 (2011).
89. H. Yoon et al., "New star pattern identification with vector pattern matching for attitude determination," *IEEE Trans. Aerosp. Electron. Syst.* **49**(2), 1108–1118 (2013).
90. K. Quirk, J. Gin, and M. Srinivasan, "Optical PPM synchronization for photon counting receivers," in *2008 IEEE Military Communications Conf. MILCOM 2008*, Vol. **4753027**(4753054), pp. 1–7, IEEE (2008).
91. S. Lin and D. J. Costello, *Error Control Coding: Fundamentals and Applications*, Vol. **114**, Pearson-Prentice Hall (2004).
92. B. Sklar, *Digital Communications*, Vol. **2**, Prentice Hall, New Jersey (2001).
93. X. Zhu and J. M. Kahn, "Communication techniques and coding for atmospheric turbulence channels," *J. Optic. Commun. Rep.* **4**(6), 363–405 (2007).
94. H. Hemmati and D. Caplan, "Optical satellite communications," in *Optical Fiber Telecommunications*, Vol. **VIB**, pp. 121–162, Systems and Networks (2013).
95. G. Ling and R. M. Gagliardi, "Slot synchronization in optical PPM communications," *IEEE Trans. Commun.* **34**(12), 1202–1208 (1986).
96. X. Sun and F. Davidson, "Timing recovery in free space direct detection optical communication systems with PPM signaling," in *IEEE Int. Conf. on Communications (ICC'89), BOSTONICC/89. Conference Record.' World Prosperity Through Communications'*, pp. 428–432, IEEE (1989).
97. X. Sun and F. M. Davidson, "Word timing recovery in direct detection optical PPM communication systems with avalanche photodiodes using a phase lock loop," *IEEE Trans. Commun.* **38**(5), 666–673 (1990).
98. F. M. Davidson and X. Sun, "Slot clock recovery in optical PPM communication systems with avalanche photodiode photodetectors," *IEEE Trans. Commun.* **37**(11), 1164–1172 (1989).
99. M. M. Willis et al., "Downlink synchronization for the lunar laser communications demonstration," in *2011 Int. Conf. on Space Optical Systems and Applications (ICSOS)*, pp. 83–87 (2011).
100. J. A. Mendenhall et al., "Design of an optical photon counting array receiver system for deep-space communications," *Proc. IEEE* **95**(10), 2059–2069 (2007).

Emily Clements is a Lincoln scholar in the Systems Engineering Group at MIT Lincoln Laboratory and a PhD student in the MIT Department of Aeronautics and Astronautics. Her work at Lincoln Laboratory has focused on the mechanical and systems engineering of a variety of experimental space systems, including laser communications payloads and small satellites. Her research focuses on uncertainty-based systems engineering methodologies for nanosatellites and their applications to laser communication.

Raichelle Aniceto is a graduate student in the MIT Department of Aeronautics and Astronautics and received a BS degree in aerospace engineering from MIT. Her research interests and background are in optical communications systems, satellite design, space radiation environment, and space systems.

Derek Barnes is a graduate student in aeronautics and astronautics at MIT. He received his undergraduate degree in aerospace engineering from MIT in 2016. His research focuses on nanosatellite optical communication systems.

David Caplan is a senior staff member in the Optical Communication Technology Group at MIT Lincoln Laboratory. His research has focused on high-sensitivity laser communication systems, with an emphasis on photon- and power-efficient transmitter and receiver design. His high-sensitivity multirate optical transceiver designs have been incorporated into NASA's deep-space interplanetary laser communication initiatives, including the Mars and lunar laser communication demonstration, and the ongoing laser communications relay demonstration program.

James Clark is a PhD student in aeronautics and astronautics at MIT. He received his undergraduate and master's degrees in aerospace engineering from MIT. His master's research focused on the application of nonlinear optics for frequency-doubling to nanosatellite laser communication; parallel to that, he worked on the optical assembly of the NODE transmitter. Currently, he is studying propulsion, trajectories, and mission plans for two MIT lasercom nanosatellite projects.

Iñigo del Portillo is a PhD student in aeronautics and astronautics at MIT. He received his BS degrees in telecommunications engineering and industrial engineering in 2014 and a MS degree in electronics engineering in 2015, all from Universitat Politecnica de Catalunya in Barcelona, Spain. His current research focuses on system architecture for optical space communication systems.

Christian Haughwout is a second-year graduate student studying aerospace engineering at MIT. He received his undergraduate degrees in chemical engineering, physics, and astronomy from the University of Massachusetts in 2015. Prior to arriving at MIT, he worked on developing particle detectors for use in Jefferson Lab's Charged Pion Polarizability Experiment. His work at MIT is focused on CubeSat design and the development of space-compatible electronics.

Maxim Khatsenko is a mechanical engineering graduate student in the STAR Lab with advisor Kerri Cahoy at MIT. He graduated from UCLA with a mechanical engineering BS in 2015, where he worked on offroad racecars with the BAJA team. His current research deals with CubeSat laser communications and CubeSat structures and deployables. His work interests include space missions and spacecraft, renewable energy, and product and machine design.

Ryan Kingsbury joined the spacecraft team at Planet in 2015 after earning a PhD and SM in aeronautics and astronautics from the Massachusetts Institute of Technology. His thesis research considered CubeSat-scale lasercom architectures, which formed the basis for the system presented in this article. Previously, he worked in satellite communications at MIT Lincoln Laboratory, and holds a BS degree in electrical engineering from Rose Hulman Institute of Technology.

Myron Lee is a second-year master's student studying aeronautics and astronautics at MIT. He received his undergraduate degree in electrical engineering from Georgia Institute of Technology. His current research projects are focused on CubeSat avionics and laser communications. In general, he is also interested in control systems and robotics applied in space.

Rachel Morgan is a third-year undergraduate student studying aerospace engineering and physics at MIT. She works in the STAR Lab on laser communications systems for CubeSats, focusing on ground station development for NODE.

Jonathan Twichell is a senior staff member in the Systems Engineering Group at MIT Lincoln Laboratory. He earned a master's and PhD in nuclear engineering from the University of Wisconsin-Madison. He joined MIT Lincoln Laboratory in 1986 helping to develop adaptive optics. He then moved to the Solid-State Division, studying wide band-gap semiconductors. He used RF photonics to extend the performance of A/D converters. Current interests include high-power coherent beam combining and small satellites.

Kathleen Riesing is a PhD student in aeronautics and astronautics at MIT studying estimation and control applied to space systems. She graduated from Princeton University in 2013 with a degree in mechanical and aerospace engineering and minors in robotics and computer science. Her MIT research has focused on pointing, acquisition, and tracking for laser communications systems on small platforms. Parallel to her work at MIT, she has interned at MIT Lincoln Laboratory, JPL, and Planet.

Hyosang Yoon is a post-quals PhD candidate in the MIT Department of Aeronautics and Astronautics. Prior to graduate school at MIT, he worked at Satrec Initiative, a commercial satellite company, as an attitude control engineer for 5 years. He has extensive experience in satellite attitude control, including onboard Kalman filter design and implementation, controller design and tuning, sensor and actuator tests, and on-orbit sensor-payload alignment calibration.

Caleb Ziegler is a second-year master's student in the MIT Department of Aeronautics and Astronautics and a Lincoln Military Fellow in Group 64 at MIT Lincoln Laboratory. He received his undergraduate degree in electrical engineering from the US Air Force Academy and is a second lieutenant in the US Air Force. His current research focuses on transmitter and receiver design for CubeSat laser communications.

Kerri Cahoy is an associate professor in the Department of Aeronautics and Astronautics at MIT. She received her BS degree (2000) in electrical engineering from Cornell University, and her MS (2002) and PhD (2008) degrees in electrical engineering from Stanford University, working with the Radio Science Team on Mars Global Surveyor. She joined the MIT faculty in July 2011 and leads the space telecommunications, astronomy, and radiation laboratory (STAR Lab).